Pointwise turbulence modelling for engineering applications

International CFD Workshop on Supersonic Transport Design
Tokyo, March 16-17 1998

U. Goldberg

Metacomp Technologies, Inc.
650 Hampshire Road, No. 200
Westlake Village, CA 91361, USA.
FAX: (805)371-8751
e-mail: ucg@metacomptech.com

Most current turbulence models involve explicit wall distance in their formulation. However, wall distance is ambiguous in all but the simplest topologies. Besides, it is not at all evident that it bears a relationship to the structure of turbulence. Thus it is desirable to base modelling practice on wall proximity indicators which are local (pointwise) in nature and convey the influence of walls indirectly, based on parameters that "measure" this proximity. Examples are the turbulence Reynolds number, $k^2/(\nu\epsilon)$, and various dot products of gradients such as $(\partial\tau/\partial x_j)(\partial k/\partial x_j)$ where $\tau = k/\epsilon$, the turbulence time scale. Adhering to this modelling practice retains full generality of the model, since the entire formulation is local. Thus wall-distance-free models are tensorially invariant and frame-indifferent, applicable to arbitrary topologies and moving boundaries. They are also usable in conjunction with solvers based on either unstructured or structured book-keeping, executed on any computer architecture, including massively parallel processors. This paper illustrates the pointwise approach to turbulence modelling by introducing several such models of both linear and nonlinear types, and by demonstrating their performance in 2D and 3D flow cases.

1 Introduction

Current and future supersonic transport vehicles incur a significant viscous drag component - as much as 20% of the total drag - and this renders Euler solvers inadequate for the design cycle. Modern designs increasingly require Navier-Stokes solvers capable of handling transitional and turbulent flows. Thus Turbulence modelling became the pacing item in CFD because it simultaneously constitutes the weakest and most influential aspect of engineering CFD. Until recently, most aerodynamic applications resorted to simple algebraic closure models of turbulence, but their inherent weaknesses under complex flow/complex topology situations - prevalent in engineering CFD - persuaded users to seek more sophisticated models, namely those involving at least one transport equation. Models such as Baldwin-Barth[1] and Spalart-Allmaras[2] are prime examples of this genre. However, both models involve explicit wall distance in their formulation, which is ambiguous in all but the simplest topologies. Equally important is the question whether wall distance has any direct influence on the structure of turbulence[3]. To avoid these issues the common strategy is to develop wall-distance-free/wall-directionality-free models which are completely topology independent, frame indifferent and tensorially invariant. The first model introduced in this paper is a

1-equation model of this type[4] which, like the Baldwin-Barth and Spalart-Allmaras models, solves directly for the undamped eddy viscosity field.

It is widely recognised, however, that better overall predictive capability for turbulent flows is possible by solving transport equations for both the length and velocity scales, giving rise to the popular k-ϵ and k-ω [5] type models or models which combine them, such as Menter's SST model [6]. Again, the majority of such models involve wall distance explicitly and the aim is to avoid this. The present paper introduces two types of wall-distance-free k-ϵ models: one aimed at predicting flows involving adverse pressure gradient[7] (both linear and nonlinear variants are presented), the other a novel k-ϵ-f_μ (3-equation) model[8] in which the low-Re damping function, f_μ, is solved from its own transport equation.

An important attribute of both the 2- and 3-equation models is time scale realisability enforcement. This means that the turbulence time scale is not permitted to become less than the corresponding Kolmogorov micro-scale. This has been proposed by Durbin[9] and by Goldberg[10, 11]. One significant outcome of enforcing time scale realisability is the automatic asymptotic consistency of the ϵ transport equation at walls, without the need to involve *ad hoc* near-wall damping functions, prevalent in many low-Re k-ϵ models[12]. This also enables a simple boundary condition for ϵ at walls. In contrast, the k-ω model uses $\omega \equiv \epsilon/k$ as the length-scale-determining variable, which is singular at walls since ϵ/k is not the correct inverse time scale there. This requires a special treatment which leads to a cumbersome and grid-dependent wall boundary condition for ω.

The models mentioned above are presented in the Appendix.

2 Highlights of the numerical approach

A Navier-Stokes solver for either compressive or incompressive flows was used in the present work. The solver features a second order Total Variation Diminishing (TVD) discretization based on a multi-dimensional interpolation framework. This framework is utilised also for the viscous terms. A Roe Riemann solver is used to provide proper signal propagation physics. Further details regarding the numerical methodology can be found in [13, 14, 15].

3 Results

In the following flow test cases the proposed models' performance is compared with experimental data and in some cases also with the GA k-ϵ model [11] which represents a more traditional k-ϵ approach. All computations were performed on a 200 MHz Pentium Pro PC. The three k-ϵ models appearing in the plots are labeled as follows: the GA model is denoted as "k-ϵ GA", the linear one as "k-ϵ τ", and the nonlinear as "k-ϵ τ quad".

3.1 *Transonic flow over an axisymmetric bump*

Mach 0.875 flow over an axisymmetric bump at $Re_\infty = 13.6 \times 10^6/\mathrm{m}$ is computed and evaluated against experimental data of Bachalo and Johnson[16]. Here a normal shock, impinging on the bump, causes flow detachment from the surface with subsequent reattachment further downstream on the cylindrical portion of the model. A sketch of the geometry, including

main flow features, is included in Figure 1(a). In Figures 1 the origin of the axial coordinate, x, is at the bump leading edge; the radial coordinate, y, originates at the axis. All lengths are scaled by the bump cord, c. Figures 1(a,b) present surface pressure coefficient (C_p) and skin friction (C_f) profiles, respectively. Figures 1(c-e) show velocity, kinetic energy, and shear stress profiles at two streamwise locations; one within the reversed flow region, the other downstream of reattachment. The computations were performed on a 151×81 grid with $y^+ \leq 1$ at the first internal node. Some streamwise clustering was also imposed, centered at $x/c = 0.7$ where the experimental shock impinges on the wall. Computation on a 181×101 grid was also performed to ascertain grid independence of the reported calculation. Figure 1(f) shows solution convergence histories, based on skin friction. Here nt is the time step counter. This approach constitutes a more stringent test than monitoring the drop in numerical residuals.

The k-ϵ-f_μ model delivers the best overall performance in this flow case. The effect of the variable C_μ, imposed by the f_μ transport equation, is seen to produce k and $\overline{uv}$ profiles which surpass even the nonlinear model in predictive quality. The latter, however, also performs quite well and predicts the mean velocity profiles best. The one-equation model overpredicts the separation bubble size and suffers from a sluggish post-reattachment recovery.

3.2 *Supersonic flow over a compression ramp*

This is the supersonic two-dimensional flow over a 24° ramp measured by Settles et al.[17], with additional data by Dolling and Murphy[18], and by Selig et al.[19]. An oblique shock, impinging on the boundary layer ahead of the ramp corner (due to upstream influence), induces flow detachment, with subsequent reattachment onto the ramp surface. A sketch, showing the geometry and some flow features, is included in Fig. 2(a). The origin of the (x, y) cartesian coordinate system is located at the ramp corner, with directions along and normal to the upstream flat plate, respectively. These coordinates are scaled by the boundary layer thickness upstream of the shock, δ_0. The computation was done on a 99×99 grid, with at least 8 cells inside the viscous sublayer, first internal node being at $y^+ < 1$. The grid was clustered in the x direction too, with $(\Delta x)_{\min} = 0.1\delta_0$, located at the ramp corner. This grid was recommended for the ETMA workshop on evaluation of turbulence models for compressive flows[20]. It has been established[18] that the shock in this flow case is unsteady, however, in the present work it was assumed to be steady in order to facilitate comparison of the models' performance.

Numerical predictions of this case are known to be strongly dependent on inflow conditions[20]. The inflow Mach number was 2.84; $Re_\infty = 7.3 \times 10^7$/m; total temperature 262 K; and static pressure 24 kPa. Wall temperature was 276K but adiabatic conditions were assumed, according to the experimental report [17]. The measured upstream boundary layer thickness, $\delta_0 = 0.023$m, was located at $x/\delta_0 = -3.0$. The computational inflow was placed at $x/\delta_0 = -21.7$ and a compressive equilibrium turbulent boundary layer (wake strength parameter $\Pi = 0.55$) of thickness $\delta_{\text{in}}/\delta_0 = 0.6$ was imposed to enable matching the measured boundary layer upstream of the strong interaction region. k_∞ was set corresponding to a freestream turbulence level $T' = 0.8\%$, and ϵ_∞ was set to a level that imposed freestream eddy viscosity on the order of the molecular viscosity. The inflow profiles of k and ϵ are given in [7].

Figs. 2(a-c) show predictions and data comparisons of surface pressure, skin friction, and corner velocity profile. Fig. 2(d) is a convergence history plot based on skin friction.

It is noted in Fig. 2(b) that the new k-ϵ models avoid the spurious post-reattachment peak typically predicted by the GA and other traditional k-ϵ models. The linear k-ϵ τ model predicts the wall pressure (Fig. 2a) only slightly better than the GA model does, but the skin friction is much better predicted by the former, and the post-reattachment branch is the best of the three models. The nonlinear k-ϵ τ model predicts the shock location much better, and also predicts the extent of flow separation considerably better than the other two models do. This is also demonstrated in predicting the corner velocity profile (Fig. 2c), indicating that the boundary layer thickness is better captured by the anisotropic model. Consequently, the oblique shock location ($y/\delta_0 \approx 1.1$) is also better predicted by this model.

3.3 *Two-hole injector*

This case corresponds to the UVA two-hole transverse injector topology. Table 2, taken from McDaniel et al.[21], shows the geometry characteristics.

Table 2

dimension	size
Diameter D	1.93
Test section height	11.03D
Test section width	15.79D
Length of measurement domain	X/D= 26.6
End of nozzle contour	X/D=-10.65
Step location	X/D= -4.94
Step height	H/D= 1.65
1st injector location	X/D= 0.0
2nd injector location	X/D= 6.58

Figure 3(a) shows a sketch of the topology, which consists of an inflow region followed by a backward-facing step after which two transverse injectors are located. The computational grid used to simulate the flowfield was derived from a fine grid (400,000 cells, Sekar[22]). This mesh was coarsened everywhere except near the hole regions and a grid with only 70,000 cells was obtained. The Mach number of the primary flow was 2.089 and that of the jets was 1.183. The flow conditions were similar to those found in McDaniel et al.[21]. The turbulence model invoked for this calculation was the 1-equation pointwise eddy viscosity model[4]. Figures 3(b-d) show pressure, streamwise velocity and vertical velocity profiles along the the 1st injector, and figures 3(e-g) are the corresponding profiles along the 2nd injector. The model enables good prediction of all profiles as compared to the experimental data[21]. Convergence for this case, using a relaxation scheme with 2 LHS forward-backward sweeps at CFL 3.0, was obtained in 1800 steps, based on five orders of magnitude drop in residuals.

4 Concluding remarks

Wall distance is ambiguous in all but the simplest topologies. On a more fundamental level, it is not at all evident that it bears a relationship to the structure of turbulence. Thus it is desirable to base modelling practice on wall proximity indicators which are local (pointwise)

in nature and convey the influence of walls indirectly, based on parameters that "measure" this proximity, such as the turbulence Reynolds number, $k^2/(\nu\epsilon)$, and various dot products of gradients like $(\partial\tau/\partial x_j)(\partial k/\partial x_j)$ where $\tau = k/\epsilon$, the turbulence time scale. Adhering to this modelling practice retains full generality, since the entire formulation is local.

This paper introduced four such models: a 1-equation R_t model, linear and quadratic variants of a k-ϵ model designed for adverse pressure gradient flow, and a 3-equation k-ϵ-f_μ model in which the damping function, f_μ, is solved from its own transport equation. Both 2-D and 3-D test cases were shown, from which it is concluded that these models can be powerful and reliable CFD tools for engineering practice.

5 Appendix: Formulation of Wall-Distance-Free Turbulence Models

5.1 1-equation model

The 1-Equation model consists of solving the following transport equation for the undamped eddy viscosity (R):

$$\frac{D(\rho R)}{Dt} = \nabla\cdot[(\mu+\mu_t/\sigma_R)\nabla R] + c_1\rho(R\mathcal{P})^{1/2} + (c_2 - c_3 f_3)\rho\nabla R\cdot\nabla R \tag{1}$$

where the production is expressed in terms of the Boussinesq model

$$\mathcal{P} = \nu_t\left[\left(\frac{\partial U_i}{\partial x_j}+\frac{\partial U_j}{\partial x_i}\right)\frac{\partial U_i}{\partial x_j} - 2/3\left(\frac{\partial U_k}{\partial x_k}\right)^2\right] \tag{2}$$

μ and μ_t are the dynamic molecular and eddy viscosities, respectively; ρ is density; $U_i = (U,V,W)$ are the cartesian velocity components; $x_i = (x,y,z)$ are the corresponding coordinates; and ν_t is the kinematic eddy viscosity, μ_t/ρ.

The eddy viscosity field is given by

$$\mu_t = f_\mu\rho R \tag{3}$$

where

$$f_\mu = \tanh\left(\alpha\chi^2\right)/\tanh\left(\beta\chi^2\right),\ \chi\equiv\rho R/\mu \tag{4}$$

The remaining near-wall function is

$$f_3 = \min\left\{1+\frac{2\alpha}{3\beta c_3\chi}, 10^5\right\} \tag{5}$$

The model constants are: $\kappa = 0.41,\ \sigma_R = 0.62,\ \alpha = 0.059,\ \beta = 0.2,$
$c_1 = \kappa^2/(2\sigma_R) = 0.1356,\ c_2 = -5\alpha/(3\beta\sigma_R) = -0.7930, c_3 = c_2 + 3/(2\sigma_R) = 1.6263$.

Equation (1) is subject to the following boundary conditions:

(i) Solid Walls

$$R = 0 \tag{6}$$

(ii) freestream and initial conditions

$$R/\nu_{\text{ref}} \le 1. \tag{7}$$

5.2 2-equation models

Reynolds stresses are related to the mean strain gradients through the quadratic model of Shih, Lumley and Zhu[23]:

$$-\rho\overline{u_i u_j} = \mu_t\left(U_{i,j}+U_{j,i}-\frac{2}{3}U_{k,k}\delta_{ij}\right)-\frac{2}{3}\rho k\delta_{ij}-\rho\frac{k^3}{\epsilon^2}\left[C_{\tau 1}(U_{i,k}U_{j,k})^*\right] \tag{8}$$
$$-\rho\frac{k^3}{\epsilon^2}\left[C_{\tau 2}(U_{i,k}U_{k,j}+U_{j,k}U_{k,i})^*+C_{\tau 3}(U_{k,i}U_{k,j})^*\right]$$

where asterisks indicate the deviatoric part; for example: $(U_{i,k}U_{j,k})^* = U_{i,k}U_{j,k}$ $- U_{m,n}U_{m,n}\delta_{ij}/3$. The coefficients in the quadratic term are

$$C_{\tau 1}=\frac{13}{1000+\overline{S}^3},\ C_{\tau 2}=\frac{-4}{1000+\overline{S}^3},\ C_{\tau 3}=\frac{-2}{1000+\overline{S}^3} \tag{9}$$

and

$$\overline{S}=\frac{k}{\epsilon}\sqrt{2S_{ij}S_{ij}},\ \overline{\Omega}=\frac{k}{\epsilon}\sqrt{2\Omega_{ij}\Omega_{ij}} \tag{10}$$

$$S_{ij}=(U_{i,j}+U_{j,i})/2,\ \Omega_{ij}=(U_{i,j}-U_{j,i})/2 \tag{11}$$

In the linear model only the first two terms on the RHS of the above stress-strain relationship are used. When using the nonlinear k-ϵ model these stresses appear directly in the viscous term of the momentum transport equation, rather than resorting to an eddy viscosity approach. However, the latter is still used in the diffusion terms of the k and ϵ transport equations. It is given by

$$\mu_t = C_\mu f_\mu \rho k^2/\epsilon \tag{12}$$

where

$$C_\mu=\frac{2/3}{1.25+\overline{S}+0.9\overline{\Omega}} \tag{13}$$

and f_μ is given by

$$f_\mu=\frac{1-e^{-A_\mu R_t}}{1-e^{-\sqrt{R_t}}}\max\{1\ ,\ \frac{C_\tau}{\sqrt{R_t}}\} \tag{14}$$

where $R_t \equiv k^2/(\nu\epsilon)$ is the turbulence Reynolds number. Full details on the derivation of f_μ are given in [11].

k and ϵ, the turbulence kinetic energy and its dissipation rate, respectively, are determined by the following transport equations.

$$\frac{\partial(\rho k)}{\partial t}+\frac{\partial}{\partial x_j}(U_j\rho k)=\frac{\partial}{\partial x_j}\left[\left(\mu+\frac{\mu_t}{\sigma_k}\right)\frac{\partial k}{\partial x_j}\right]+P_k-\rho\epsilon \tag{15}$$

$$\frac{\partial(\rho\epsilon)}{\partial t}+\frac{\partial}{\partial x_j}(U_j\rho\epsilon)=\frac{\partial}{\partial x_j}\left[\left(\mu+\frac{\mu_t}{\sigma_\epsilon}\right)\frac{\partial\epsilon}{\partial x_j}\right]+(C_{\epsilon 1}P_k-C_{\epsilon 2}\rho\epsilon+E)T_t^{-1} \tag{16}$$

P_k is the turbulence production, $-\rho\overline{u_i u_j}U_{i,j}$, used in exact form in the nonlinear model, but modelled in terms of the Boussinesq concept in the linear one:
$P_k = \left[\mu_t\left(U_{i,j}+U_{j,i}-\frac{2}{3}U_{k,k}\delta_{ij}\right)-\frac{2}{3}\rho k\delta_{ij}\right]U_{i,j}$.

The realisable time scale is

$$T_t = \frac{k}{\epsilon} \max\{1 \ , \ \frac{C_\tau}{\sqrt{R_t}}\} \tag{17}$$

This time scale is k/ϵ at large R_t but becomes proportional to the Kolmogorov scale, $\sqrt{\nu/\epsilon}$, for $R_t \ll 1$. Reference [11] includes full details about this time scale, whose inclusion guarantees near-wall asymptotic consistency of the ϵ equation without resorting to *ad hoc* damping functions (see [12] for example).

The extra source term, E, is designed to increase the level of ϵ in non-equilibrium flow regions, thereby reducing the length scale and enabling improved prediction of adverse pressure gradient flows, including those involving backflow regions:

$$\Psi = \max\left\{ \frac{\partial k}{\partial x_j}\frac{\partial \tau}{\partial x_j}, 0 \right\} \tag{18}$$

$$\mathcal{V} = \max\left\{ k^{1/2}, (\nu\epsilon)^{1/4} \right\} \tag{19}$$

$$E = A_E \rho \mathcal{V} \sqrt{\epsilon T_t}\Psi \tag{20}$$

where $\tau = k/\epsilon$, the turbulence time scale. The extra source term is invoked only in near-wall regions, where $\Psi > 0$. Note the realisable velocity scale, $\mathcal{V}$, whose presence limits the influence of E to a relatively small fraction of the boundary layer near walls, with a sharp cut-off further away. Finally, the model constants are $C_{\mu_{\text{linear}}} = 0.09$, $C_{\epsilon 1} = 1.44$, $C_{\epsilon 2} = 1.92, \sigma_k = 1.0$, $\sigma_\epsilon = 1.3$, $A_\mu = 0.01$, $A_{E_{\text{linear}}} = 0.35$, $A_{E_{\text{nonlinear}}} = 0.15$, $C_\tau = \sqrt{2}$.

The two transport equations, Eqs. (15) and (16), are subject to the following boundary conditions at solid walls. The kinetic energy of turbulence and its first normal-to-wall derivative vanish at walls. The former condition is implemented directly:

$$k_{\text{w}} = 0 \tag{21}$$

The boundary condition for ϵ is based on its near-wall asymptotic behaviour ($y \to 0$):

$$\epsilon_{\text{w}} = 2\nu_1 \frac{k_1}{y_1^2} \tag{22}$$

where "1" denotes the first internal node. This boundary condition implies that $(\partial k/\partial y)_{\text{w}} = 0$, satisfying the second boundary condition for k implicitly.

5.3 3-equation model

Reynolds stresses are related to the mean strain through the Boussinesq model:

$$-\rho\overline{u_i u_j} = \mu_t \left(U_{i,j} + U_{j,i} - \frac{2}{3} U_{k,k}\delta_{ij} \right) - \frac{2}{3}\rho k \delta_{ij} \tag{23}$$

where the eddy-viscosity field is given by

$$\mu_t = f_\mu \rho k^2/\epsilon \tag{24}$$

Here k, ϵ, and f_μ, the turbulence kinetic energy, its dissipation rate, and the damping function, respectively, are determined by the following transport equations.

$$\frac{\partial(\rho k)}{\partial t} + \frac{\partial}{\partial x_j}(U_j \rho k) = \frac{\partial}{\partial x_j}\left[\left(\mu + \frac{\mu_t}{\sigma_k}\right)\frac{\partial k}{\partial x_j}\right] + P_k - \rho\epsilon \tag{25}$$

$$\frac{\partial(\rho \epsilon)}{\partial t} + \frac{\partial}{\partial x_j}(U_j \rho \epsilon) = \frac{\partial}{\partial x_j}\left[\left(\mu + \frac{\mu_t}{\sigma_\epsilon}\right)\frac{\partial \epsilon}{\partial x_j}\right] + (C_{\epsilon 1} P_k - C_{\epsilon 2}\rho\epsilon) T_t^{-1} \tag{26}$$

$$\frac{\partial(\rho f_\mu)}{\partial t} + \frac{\partial}{\partial x_j}(U_j \rho f_\mu) = \frac{\partial}{\partial x_j}\left[\left(\mu + \frac{\mu_t}{\sigma_f}\right)\frac{\partial f_\mu}{\partial x_j}\right] + \mu \frac{\partial f_\mu}{\partial x_j}\frac{\partial f_\mu}{\partial x_j} - [A_\mu \rho (C_\mu - f_\mu)]^2 \frac{k}{\mu} \tag{27}$$

P_k is the turbulence production, $-\rho\overline{u_i u_j} U_{i,j}$, modelled in terms of the Boussinesq concept (23). The realisable time scale, T_t, is the same as in the 2-equation models. Details about Eq. (27) are found in [8]. The model constants are: $C_\mu = 0.09$, $C_{\epsilon 1} = 1.44$, $C_{\epsilon 2} = 1.92$, $\sigma_\epsilon = 1.3$, $\sigma_k = 1.0$, $\sigma_f = 50.0$, $A_\mu = 0.001$.

The three transport equations, Eqs. (25-27), are subject to the following boundary conditions at solid walls. The ones for k and ϵ are the same as in the 2-equation models, and the boundary condition for the damping function is $f_{\mu_w} = 0$. Freestream/initial condition is $f_\mu = C_\mu$.

References

[1] Baldwin, B.S. and Barth, T.J. (1990) A one-equation turbulence model for high Reynolds number wall bounded flows, NASA TM-102847.

[2] Spalart, P.R. and Allmaras, S.R. (1994) A one-equation tubulence model for aerodynamic flows, *La Recherche Aerospatiale* **1** 5.

[3] Launder, B.E. (1988) On the computation of convective heat transfer in complex turbulent flows, *ASME J. Heat Transfer* **110**, 1112.

[4] Goldberg, U.C. (1996) A pointwise one-equation turbulence model for wall bounded and free shear flows, *Turbulence, Heat and Mass Transfer 1*, K. Hanjalic and J.C.F. Pereira *Eds.*, Begell House, Inc., 209.

[5] Wilcox, D.C. (1993) *Turbulence modeling for CFD*, DCW Industries, Inc., La Cañada, California.

[6] Menter, F.R. (1993) Zonal two equation k-ω turbulence models for aerodynamic flows, AIAA Paper 93-2906.

[7] Goldberg, U., Peroomian, O. and Chakravarthy, S. (1998) A wall-distance-free k-ϵ model with enhanced near-wall treatment, to be published in ASME *J. Fluids Engrg.*.

[8] Goldberg, U. and Palaniswamy, S. (1998) The k-ϵ-f_μ turbulence closure model, in review, *Computer Meth. Appl. Mech. Engrg.*

[9] Durbin, P.A. (1991) Near-wall turbulence closure modeling without 'damping functions', *Theoretical and Computational Fluid Dynamics* **3** 1.

[10] Goldberg, U.C. (1991) Derivation and testing of a one-equation model based on two time scales, *AIAA Journal* **29** 1337.

[11] Goldberg, U. and Apsley, D. (1997) A wall-distance-free low Re k-ϵ turbulence model, *Computer Meth. Appl. Mech. Engrg.* **145** 227.

[12] Lam, C.K.G. and Bremhorst, K.A. (1981) Modified form of k-ϵ model for predicting wall turbulence, ASME *J. Fluids Engrg.* **103** 456.

[13] Chakravarthy, S., Peroomian, O. and Sekar, B. (1996) Some internal flow applications of a unified-grid CFD methodology, AIAA Paper 96-2926.

[14] Peroomian, O., Chakravarthy, S. and Goldberg, U. (1997) A "grid-transparent" methodology for CFD, AIAA Paper 97-07245.

[15] Peroomian, O., Chakravarthy, S., Palaniswamy, S. and Goldberg, U. (1998) Convergence acceleration for unified-grid formulation using preconditioned implicit relaxation, AIAA Paper 98-0116.

[16] Bachalo, W.D. and Johnson, D.A. (1979) An investigation of transonic turbulent boundary layer separation generated on an axisymmetric flow model, AIAA Paper 79-1479.

[17] Settles, G.S., Fitzpatrick, T.J., and Bogdonoff, S.M. (1979) Detailed study of attached and separated compression corner flowfields in high Reynolds number supersonic flow, *AIAA Journal* **17**, No. 6, 579.

[18] Dolling, D.S. and Murphy, M.T. (1983) Unsteadiness of the separation shock wave structure in a supersonic compression ramp flowfield, *AIAA Journal* **21**, No. 12, 1628.

[19] Selig, M.S., Andreopoulos, J., Muck, K.C., Dussauge, J.P., and Smits, A.J. (1989) Turbulence structure in a shock wave/boundary layer interaction, *AIAA Journal* **27**, No. 7, 862.

[20] Loyau, H. and Vandromme, D. (1994) TC5 Workshop Synthesis. In *Proc. of ETMA Workshop* UMIST, Manchester, U.K.

[21] McDaniel, J., Fletcher, D., Hartfield, R. Jr., and Hollo, S. (1991) Staged transverse injection into Mach 2 flow behind a rearward-facing step: a 3-D compressible test case for hypersonic combustor code validation, AIAA Paper 91-5071.

[22] Sekar, B. (1995) Three dimensional computation of parallel and non-parallel injection in supersonic flow, AIAA Paper 95-0886.

[23] Shih, T.H., Lumley, J.L. and Zhu, J. (1993) A realizable Reynolds stress algebraic equation model, NASA TM-105993.

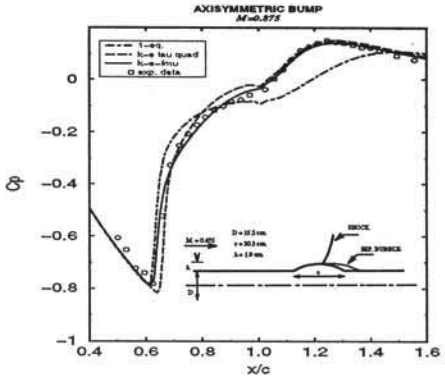

Fig. 1(a) Surface pressure distribution

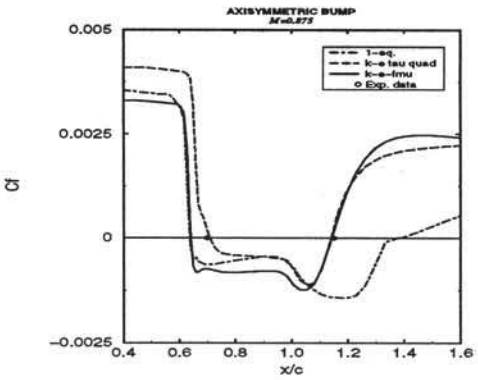

Fig. 1(b) Skin friction distribution

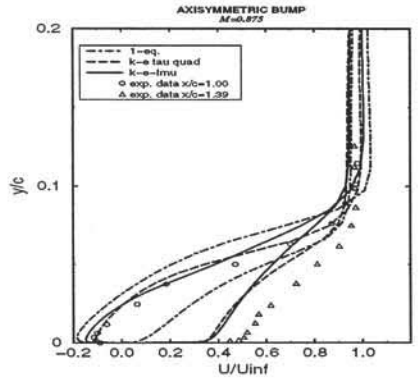

Fig. 1(c) Streamwise velocity profiles

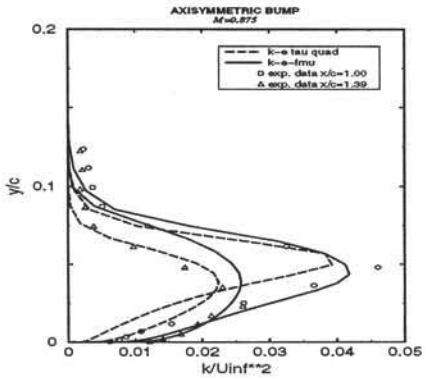

Fig. 1(d) Turbulence kinetic energy profiles

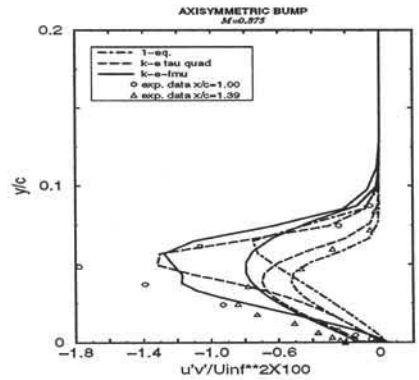

Fig. 1(e) Shear stress profiles

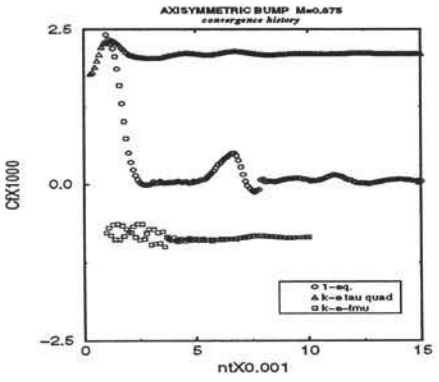

Fig. 1(f) Solution convergence history

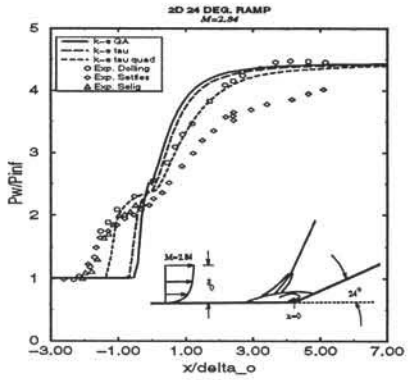

Fig. 2(a) Surface pressure distribution

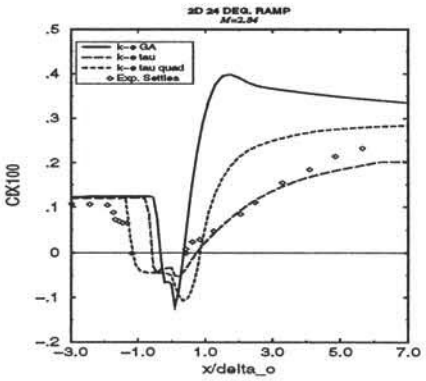

Fig. 2(b) Skin friction distribution

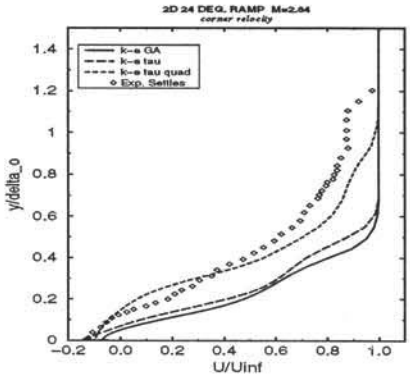

Fig. 2(c) Corner velocity profiles

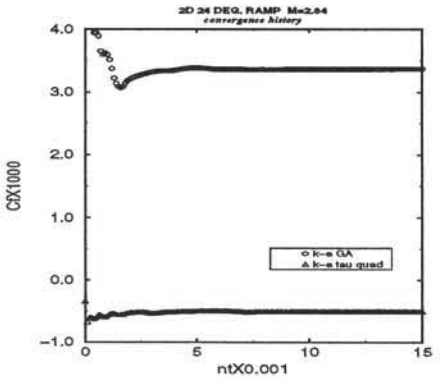

Fig. 2(d) Solution convergence history

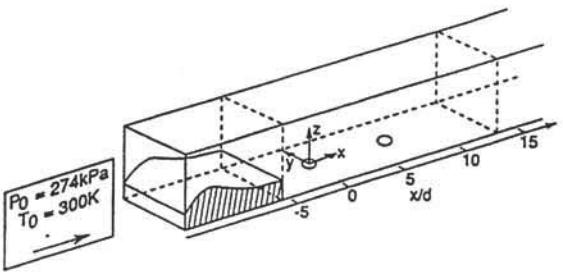

Fig. 3(a) UVA two-hole injector geometry (Courtesy D.R. Eklund, NASA LaRC)

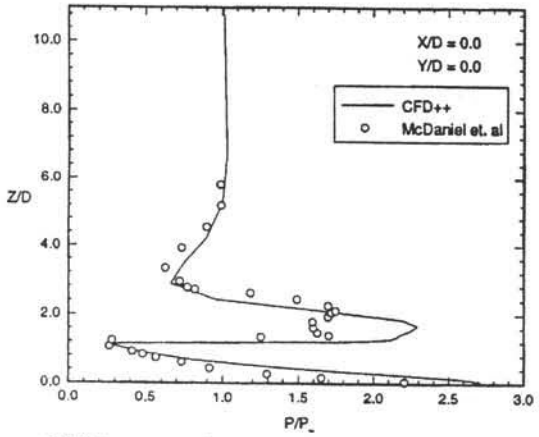

Figure 3(b) Pressure along the centerline of first injector.

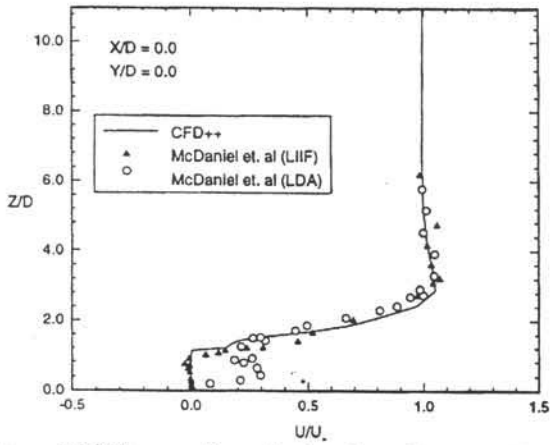

Figure 3(c) Streamwise velocity along the centerline of first injector.

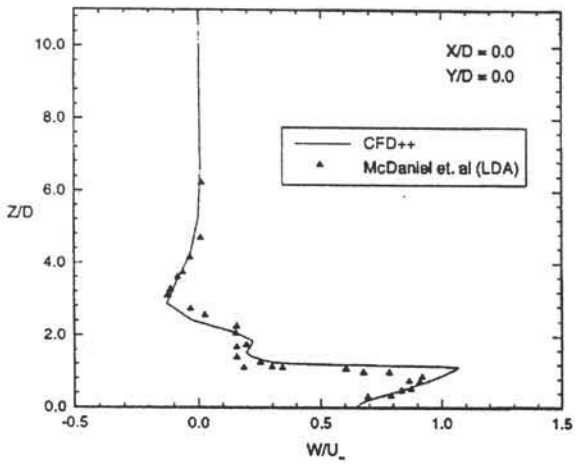

Figure 3(d) Vertical velocity along the centerline of first injector.

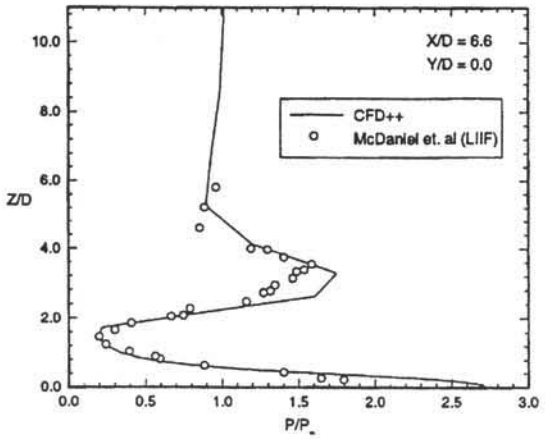

Figure 3(e) Pressure along the centerline of second injector.

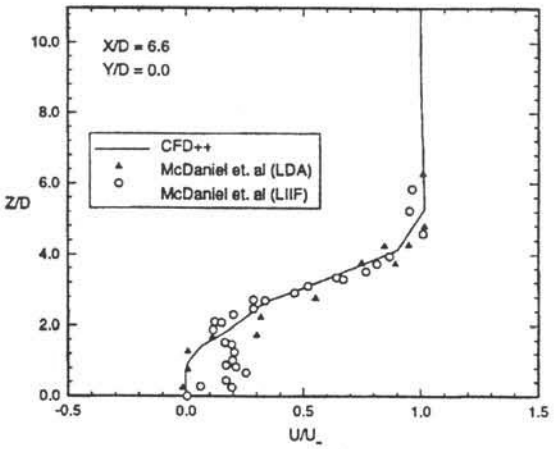

Figure 3(f) Streamwise velocity along the centerline of second injector.

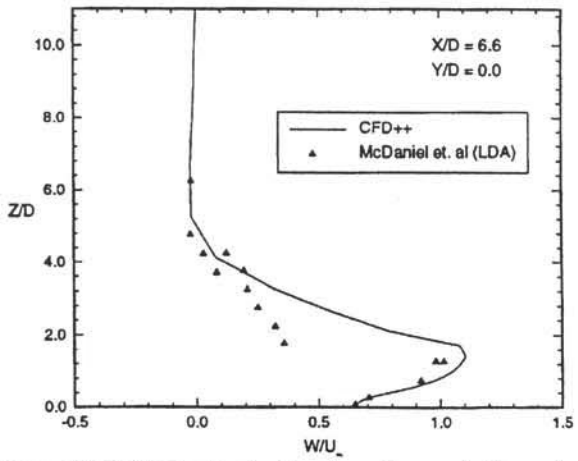

Figure 3(g) Vertical velocity along the centerline of second injector.